Modeling of Empirical Transfer Functions with 3D Velocity Structure

Zhifeng Hu[*1,2], Daniel Roten[1], Kim B. Olsen[1], and Steven M. Day[1]

ABSTRACT

Empirical transfer functions (ETFs) between seismic records observed at the surface and depth represent a powerful tool to estimate site effects for earthquake hazard analysis. However, conventional modeling of site amplification, with assumptions of horizontally polarized shear waves propagating vertically through 1D layered homogeneous media, often poorly predicts the ETFs, particularly, in which large lateral variations of velocity are present. Here, we test whether more accurate site effects can be obtained from theoretical transfer functions (TTFs) extracted from physics-based simulations that naturally incorporate the complex material properties. We select two well-documented downhole sites (the KiK-net site TKCH05 in Japan and the Garner Valley site, Garner Valley Downhole Array, in southern California) for our study. The 3D subsurface geometry at the two sites is estimated by means of the surface topography near the sites and information from the shear-wave profiles obtained from borehole logs. By comparing the TTFs to ETFs at the selected sites, we show how simulations using the calibrated 3D models can significantly improve site amplification estimates as compared to 1D model predictions. The primary reason for this improvement in 3D models is redirection of scattering from vertically propagating to more realistic obliquely propagating waves, which alleviates artificial amplification at nodes in the vertical-incidence response of corresponding 1D approximations, resulting in improvement of site effect estimation. The results demonstrate the importance of reliable calibration of subsurface structure and material properties in site response studies.

KEY POINTS

- We propose a 3D modeling method to improve conventional 1D site response.
- The shallow 3D structure used by the method can be refined using surface topography.
- A 3D model redirects vertically propagating waves to more realistic obliquely propagating waves.

Supplemental Material

INTRODUCTION

Details of how ground shaking is affected by near-surface soil properties can help reduce the uncertainty in stochastic or empirical ground-motion models, which are important components of seismic hazard calculations. Transfer functions (TFs) are widely used to quantitatively represent site response by computing the spectral ratio of ground motions between site and reference locations in the frequency domain (e.g., Shearer and Orcutt, 1987; Steidl, 1993; Field and Jacob, 1995; Steidl *et al.*, 1996; Bonilla *et al.*, 2002). Assuming that the reference site, while sharing, approximately, the same path and source with the site of interest, is largely unaffected by site effects, the spectral ratio provided by the TF isolates the site response (Borcherdt, 1970). Two types of reference sites, both typically rock, have been proposed: a surface site or a downhole recording (used with the corresponding surface site). The surface-downhole record pair is valuable for ensuring close proximity of the reference motions at the downhole sensor, ideally located in bedrock, whereas, it may be difficult to find an appropriate reference outcrop site within close distance to the soil site. In this article, we will only analyze TFs computed using surface-downhole site pairs.

The accuracy of site response estimates depends on the accuracy of the subsurface model used, and this is usually assumed to be controlled by the uncertainty in the site properties, in particular, the shear-wave velocity, V_S (Barani *et al.*, 2013; Griffiths *et al.*, 2016). V_S is the most important parameter for conventional 1D modeling of the TF, in which it is

1. Department of Geological Sciences, San Diego State University, San Diego, California, U.S.A.; 2. Institute of Geophysics and Planetary Physics, Scripps Institution of Oceanography, University of California, San Diego, La Jolla, California, U.S.A.

*Corresponding author: zhh076@ucsd.edu

Cite this article as Hu, Z., D. Roten, K. B. Olsen, and S. M. Day (2021). Modeling of Empirical Transfer Functions with 3D Velocity Structure, *Bull. Seismol. Soc. Am.* **XX**, 1–15, doi: 10.1785/0120200214

assumed that surface (and subsurface) motion consists of horizontally polarized plane *S* waves propagating through a stack of homogeneous layers (Kramer, 1996). This modeling procedure (SH1D) ignores the lateral complexity of the often heterogeneous geology and subsurface structure and is, therefore, not able to include potential 2D and 3D amplification effects in the observations (e.g., Roten *et al.*, 2008; Thompson *et al.*, 2012). Zhu *et al.* (2018) performed numerical analysis on 2D basins and found that a constant spectral aggravation factor (Chávez-García and Faccioli, 2000), which quantifies the discrepancy between 1D and 2D/3D models, is insufficient to identify basin effects, especially, in close-to-edge regions of shallow basins. Both observations and analytical solutions suggest that 1D models lack an estimate of spatial variability, caused by complex wave propagation such as basin amplification, surface-wave generation, and scattering, and are, therefore, unable to capture spatial correlations, which may be important for understanding risk, especially, to regional-scale infrastructure (e.g., Olsen and Schuster, 1995; Boore, 2004). Although, recent approaches have attempted to reduce velocity uncertainties in site effect estimation (Matavosic and Hashash, 2012; Teague *et al.*, 2018), these methods either require prohibitively complex processing or are developed for specific cases only.

It is impractical to constrain subsurface structure over a wide region to the resolution (on the order of meters to tens of meters) required for accurate ground-motion estimation to high frequencies (e.g., 10 Hz). Instead, some studies choose to use simple proxies, based on broad site classes to supplement estimates of soil properties and site spatial characteristics, for example, the National Earthquake Hazards Reduction Program (NEHRP) soil classification (Building Seismic Safety Council [BSSC], 2003; Akkar and Bommer, 2010) or a weighted average of V_S in the uppermost 30 m (V_{S30}, e.g., Abrahamson and Silva, 2008; Idriss, 2014). Thompson *et al.* (2012) proposed a scheme to classify surface-downhole site pairs by the extent of interevent variability and goodness of fit between 1D modelling and empirical site response, which can be used to calibrate the constitutive models and guide specific site studies. Despite the use of these characterizations in some generic seismic hazard estimates, for instance, via ground-motion prediction equations, recent work has pointed out the importance of considering site-to-site amplification variability (Atkinson and Boore, 2006; Atik *et al.*, 2010). These studies show that, even within a single NEHRP or V_{S30} class, the variability of site amplification and spatial correlations is strong enough to contribute significant uncertainty in ground-motion estimates.

In this article, we propose a method to constrain the near-surface properties using surface topography and perform high-resolution 3D numerical simulations to investigate the uncertainty in site response modeling. The simulations naturally take advantage of 3D geotechnical information and are able to incorporate complicated spatially varying amplification effects. We use two downhole array sites, namely the Garner Valley Downhole Array (GVDA) in California and the TKCH05 site from the Kiban–Kyoshin network (KiK-net) surface-downhole pairs in Japan, where detailed in situ constraints of site seismic properties (e.g., V_S and layer thicknesses) and abundant earthquake records are available, for our analysis. Both borehole sites have well-documented geological structure data, and previous studies have showed that SH1D modeling poorly predicts the ground motions without adjustments of subsurface properties or recalibration of constitutive models. Thompson *et al.* (2012) found low interevent variability and poor fit using SH1D modeling for the site TKCH05, due to omission of spatial variability around the site that scatters the downgoing waves and reduces pseudoresonance. They found that no satisfactory fit could be achieved by adjusting the velocity profile, whereas Tao and Rathje (2020) showed that modification in the top 20 m can significantly improve the site response estimate for the outcrop TF (spectral ratio between two surface sites). Bonilla *et al.* (2002) studied the wave propagation at GVDA and reported significant *S*-to-*P* conversions that led to misfit in prediction of the empirical TF (ETF; see the TFs section) by horizontal-to-vertical spectral ratios. Teague *et al.* (2018) applied the Toro randomization model (Toro, 1995) with the spectral analysis of surface waves method, to obtain the site signature with the best match of the ETF and the theoretical TF (TTF); however, this approach suffers from the nonunique nature of inverting V_S profiles.

DATA

Dependent on the strength of the input motion, site amplification and deamplification can be caused by a combination of linear and nonlinear effects. Here, we focus on linear site effects, and reserve the nonlinear analysis for subsequent research endeavors. To limit our analysis to linear ground motions, we exclude records with maximum surface accelerations larger than 0.1*g* (e.g., Beresnev and Wen, 1996). For each of the two site selections, we randomly picked 36 events of various azimuth and distance to the site that meets this criterion, with a minimum signal-to-noise ratio of five in their records. The goodness of fit between TTFs and ETFs from recordings is described by the variance reduction (VR) as follows:

$$\mathrm{VR} = 1 - \frac{\sum_{i=1}^{n}[\mathrm{TTF}(f_i) - \mathrm{ETF}_{\mathrm{med}}(f_i)]^2}{\sum_{i=1}^{n}[\mathrm{ETF}_{\mathrm{med}}(f_i)]^2}, \qquad (1)$$

in which n is the number of frequencies at which the ETFs and TTFs are computed, and $\mathrm{ETF}_{\mathrm{med}}$ is the median of the ETFs from the events that we selected. We evaluate a set of linearly spaced frequencies between 0.5 and 10 Hz, with the lower limit determined by the noise level of the data, and the upper limit from the resolution of our simulations. The VR ranges within $[-\infty, 1]$, in which VR = 1 means a perfect match, and smaller values indicate poorer fit.

TFs

We compute TFs between surface and downhole locations as follows:

$$\mathrm{TF} = \frac{G_s(f)}{G_d(f)}, \tag{2}$$

in which $G_s(f)$ and $G_d(f)$ are the root mean squares of the Fourier amplitude spectra of horizontal accelerations at the surface and downhole locations, respectively. It is worthwhile to note that the downhole recordings include the upgoing incident wavefield as well as downgoing waves that are reflected back from the free surface. This phenomenon complicates the wavefields recorded at downhole sites, and, therefore, the use of surface-downhole pairs to study site response. For records obtained at depths shallower than 200 m, as in this study, the upgoing and downgoing pulses overlap in the records, with differences in arrival times as small as 0.2 s, complicating a separation of the two contributions in the presence of extended source duration and site response (Shearer and Orcutt, 1987). For example, Bonilla *et al.* (2002) found from simulations at the GVDA site using the f-k method that the downgoing wave effect is predominant above the soil-bedrock interface and strongly degraded below that depth. Because it is almost impossible to eliminate downgoing waves from the records, we include the total wavefields at the surface and downhole sites, when calculating the TFs for both synthetics and records.

Our procedure for processing the recorded time series is similar to that documented in Tao and Rathje (2019). First, we collected acceleration time series at the surface and downhole accelerometers. Second, a fifth-order Butterworth filter, with a passband of 0.5–12 Hz, was applied to the demeaned and detrended accelerations, in which signal at frequencies below 0.5 Hz was discarded to minimize the contribution from low-frequency noise interference. Third, a second-order polynomial baseline correction was applied to the observed displacement time series, obtained by integrating the accelerations twice. Then, the ETFs were obtained as the ratio of the Fourier spectral amplitude between the surface and downhole acceleration time series for all the events. We further smoothed the TFs using the Konno–Ohmachi smoothing window in the frequency domain (Konno and Ohmachi, 1998). Although, not necessary for the synthetics, we applied the preprocessing (steps 2 and 3) to both synthetics and data for consistency.

MODEL CONSTRUCTION

It is reasonable to assume that, in the vicinity of a site of interest, bedrock depth varies in accordance with surface topography. In such models, sites located in a mountainous area have near-zero bedrock depth, whereas, sites in valley regions are characterized by larger depths to bedrock. Under this assumption, our 3D mesh is generated by mapping the topography to bedrock depth, with the constraints from borehole logging measurements. Oftentimes, bedrock depth increases rapidly from the edge toward the center of a sedimentary valley and approaches a maximum near the center of the valley, suggesting that depth to bedrock in a valley can be estimated using the topographic signature from digital elevation models. Gallant and Dowling (2003) proposed an algorithm that operates at multiple scales and combines topographic elevations into a single continuous multiresolution index of valley bottom flatness (MRVBF). Values of MRVBF below 0.5 represent areas with the steepest topography, values between 0.5 and 1.5 relate to the steep areas with few flat valley bottoms, and larger MRVBF values indicate broader and flatter valley bottoms. Here, we adopt the MRVBF technique and used the same threshold value (1.5) as in Gallant and Dowling (2003), to discriminate valley and mountainous regions. The quantitative relationship between the bedrock depth (D) and MRVBF values are assumed to obey a logarithmic formula:

$$D = \max\left(0, D_0 \times \log_{10}\left(\frac{\mathrm{MRVBF}}{\mathrm{MRVBF}_t}\right)\right), \tag{3}$$

in which MRVBF_t is the threshold MRVBF value (here, 1.5), and D_0 is a coefficient, which is calculated by substituting the MRVBF value and bedrock depth at the borehole site into the equation, that is, $D_0 = D_{\mathrm{borehole}} / \log_{10}(\frac{\mathrm{MRVBF}_{\mathrm{borehole}}}{\mathrm{MRVBF}_t})$.

In addition to the modifications of the velocity model from the MRVBF method, we explore the extent to which scattering effects from statistical distributions of near-surface small-scale heterogeneities (SSHs) can improve site effect estimation. Previous studies using 1D modeling show that including SSHs may improve the prediction of ETFs, likely by weakening the downgoing wave effects (Nour *et al.*, 2003; Thompson *et al.*, 2012). Here, we use guidance from published studies on spectral coloring of Gaussian random numbers with von Karman spatial correlation functions for characterizing the statistics of heterogeneities (see Appendix; as well as, e.g., Frankel and Clayton, 1986; Savran and Olsen, 2019; Withers *et al.*, 2019). We use a Hurst number of 0.05, a correlation length of 100 m, a standard deviation of 5%, and a horizontal-to-vertical anisotropy of five, as constrained from sonic borehole logs in the Los Angeles basin by Savran and Olsen (2016). We include SSHs with these parameters, when generating TFs at our two selected locations, whereas, the sensitivity of the TFs to variation in the parameters is explored in the Discussion section.

Numerical simulations

Our goal to quantify the effects of 3D Earth structure on high-frequency (<10 Hz) TFs, using 3D modeling, is computationally challenging. We use the parallel and scalable discontinuous-mesh velocity–stress staggered-grid finite-difference code AWP-ODC-DM (Olsen, 1994; Cui *et al.*, 2010; Nie *et al.*, 2017) to simulate the site response. One-dimensional TTFs are computed under the SH1D assumption, in which the model consists of a stack of homogeneous layers, to provide a point of

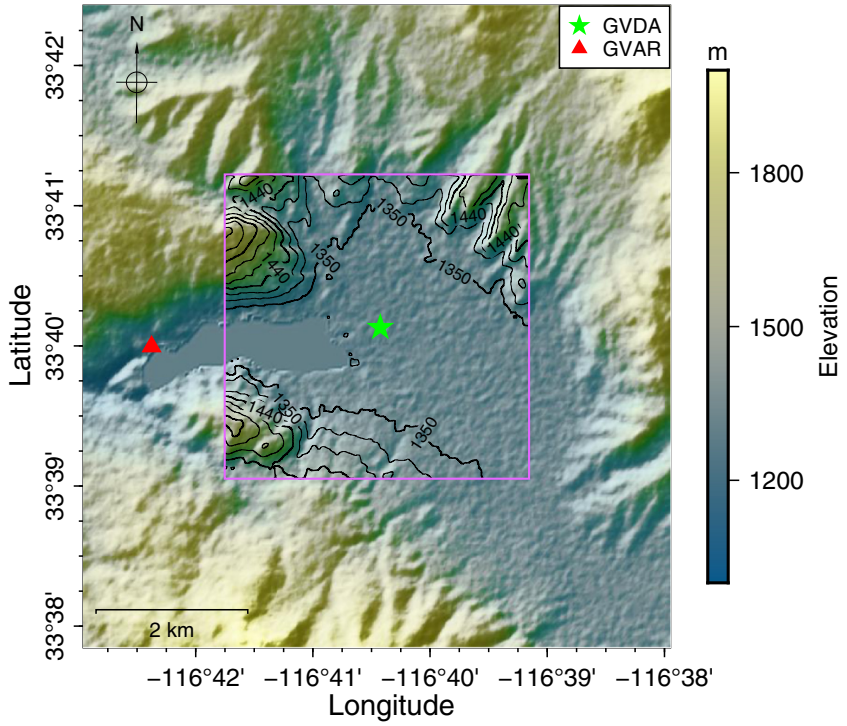

Figure 1. Site map of Garner Valley Downhole Array (GVDA), denoted by the star. The rectangle depicts the extent of the modeling domain, where the contours depict elevation in meters. The triangle denotes a nearby outcrop site GVAR. The color version of this figure is available only in the electronic edition.

comparison for the 3D models. The model definition for the 3D TTF computation is more complicated. We include the effects of frequency-dependent attenuation using the model:

$$Q(f) = \begin{cases} Q_0 \times f^{\gamma}, & f > 1 \\ Q_0, & f \le 1 \end{cases}, \tag{4}$$

in which Q_0 is a frequency-independent constant attenuation proportional to the velocity, and γ is a power-law exponent describing the attenuation above 1 Hz (Withers *et al.*, 2015). Here, we adopt area-specific parameters suggested in the literature; for GVDA, we use $Q_{s,0} = 0.05 \times V_S$ (V_S in meters per second), $Q_{p,0} = 2 \times Q_{s,0}$, and $\gamma = 0.6$ (Withers *et al.*, 2015, for southern California), and for TKCH05, we use a model for $Q_{p,0} = Q_{s,0} = Q_0$, given by

$$Q_0 = \begin{cases} 60, & V_S \le 600 \\ 100, & 600 < V_S \le 1100 \\ 150, & 1100 < V_S \le 2100 \\ 200, & 2100 < V_S \le 3200 \\ 300, & V_S > 3200 \end{cases}, \tag{5}$$

in which V_S is in meters per second, from the Japan Seismic Hazard Information Station (J-SHIS) and $\gamma = 0.2$, following the study by Nakajima *et al.* (2013). We discretize the velocity models using two partitions in our discontinuous mesh, with grid spacings small enough to resolve the minimum V_S wavelengths (20 m and 14 m for the GVDA and TKCH05 cases, respectively), anywhere in the model with, at least, five points. In our simulations, the surface recordings at a neighboring outcrop site are deconvolved from its local subsurface property layers, up to the bottom of the simulation domain; the resulting three-component acceleration time series (converted to body forces in AWP-ODC-DM) are then distributed on the entire bottom surface of the computational domain, to generate a one-way upward propagating plane wave. We verified that such vertical-incident plane wave sources are reasonable approximations, considering our shallow simulation domains (0.4 km and 1 km deep at GVDA and TKCH05, respectively), as well as earthquake hypocenters at depths of 10 km+ and distances of tens of kilometers. We used an elastic boundary condition at the bottom grid boundary, which is transparent to downgoing waves, to avoid artificial resonance of the soil column (Roten *et al.*, 2012). We part from the common way of placing the model base at the downhole site and have the input motion as the downhole motion, due to our boundary conditions. We perform the numerical simulations on the Oak Ridge National Laboratory Summit supercomputer, in which each of our simulations with the 3D model at TKCH05, including 64 million cells, requires a wall-clock time of 100 min on 32 graphic processing units for 750,000 timesteps. Similar computational requirements are needed for the 3D GVDA simulations.

GVDA

The GVDA is located in a seismically active region of California, 7 km from the San Jacinto fault and 35 km from the San Andreas fault (Archuleta *et al.*, 1992; see Fig. 1). The site is situated in a narrow valley within the Peninsular Ranges Batholith (Bonilla *et al.*, 2002), 23 km east of Hemet and 20 km southwest of Palm Springs, California. The near-surface stratigraphy beneath GVDA consists of extensive lake-bed alluvium and decomposed crystalline rocks (Hill, 1981). Soft silty and clayey sands makes up the top 18–25 m across the site (Steidl *et al.*, 1996), followed by 50–60 m thick, decomposed,

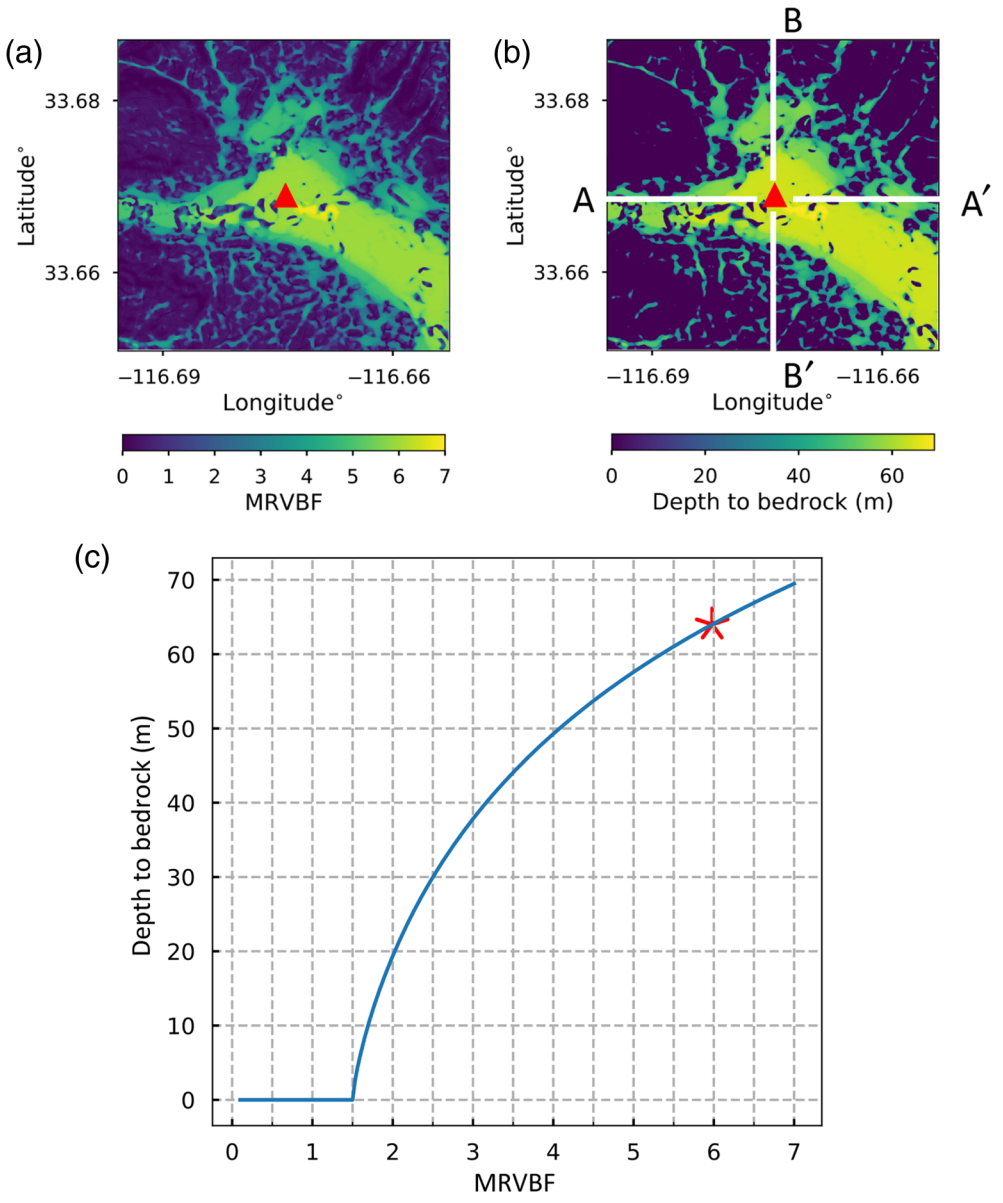

Figure 2. (a) Multiresolution index of valley bottom flatness (MRVBF) and (b) the bedrock depth map surrounding GVDA, which is depicted by a triangle in both figures. (c) The mapping function from MRVBF to bedrock depth, with GVDA marked with an asterisk. The color version of this figure is available only in the electronic edition.

and weathered granite down to about 64–87 m, as constrained by seismic downhole testing and shallow and deep *P*–*S* velocity suspension logging (Gibbs, 1989; Steller, 1996). The GVDA site is equipped with multiple downhole accelerometers, at depths of 15, 22, 50, and 150 m that are capable of measuring accelerations from 3×10^{-6} to 2.0*g* below 100 Hz. The 150 m deep accelerometer is the only downhole sensor that penetrates the granitic rock, which is used to compute TTFs in this study.

To be able to resolve frequencies up to 10 Hz at the GVDA site, we generated a mesh of size 4 km × 4 km × 0.4 km (length × width × depth), with mesh properties compressional wave velocity (V_P), V_S and density from the 3D Community Velocity Model (CVM) S4.26.M01, which is developed and maintained by the Southern California Earthquake Center (SCEC; Small *et al.*, 2017). The borehole logs show V_S of the near-surface soft soils between 180 and 220 m/s, with the value of V_S smaller than 200 m/s only at depths between 1.4 and 2.8 m (Steller, 1996). The minimum velocity in our model was truncated at 200 m/s, which is about the average of the top 4 m, resolving frequencies up to 10 Hz, with, at least, five points per minimum *S* wavelength, using a smallest grid spacing of 4 m. The SCEC CVM S4.26.M01, however, fails to resolve the 3D Garner Valley structure to the accuracy required by our analysis, and we use the MRVBF method to describe the depth to bedrock instead.

At every surface location, we first compute the MRVBF value and bedrock depth, as described in the Numerical simulations section. We then force the V_P, V_S, and densities above the bedrock to be the same as those in the measured borehole log, while keeping the seismic velocities and densities unchanged in the bedrock. Figure 2 illustrates how we estimate bedrock depth from the MRVBF values, using surface topography. The deeper parts of the valley are represented by larger MRVBF values. The areas with MRVBF smaller than the threshold value at 1.5 are shown in dark shading, corresponding to steeper terrain. The borehole site GVDA, at the center of the region, has a MRVBF value of 5.8 and bedrock depth of 64 m, consistent with the borehole log from Gibbs (1989). The 3D geometry inferred from the spatially varying bedrock depth is shown in the left panels of Figure 3, compared to the original borehole profile in the right panel.

Although we computed the ETFs for all the selected 36 events (Table 1, Fig. S1, available in the supplemental material to this article), only one event (ID = 33) was used to generate

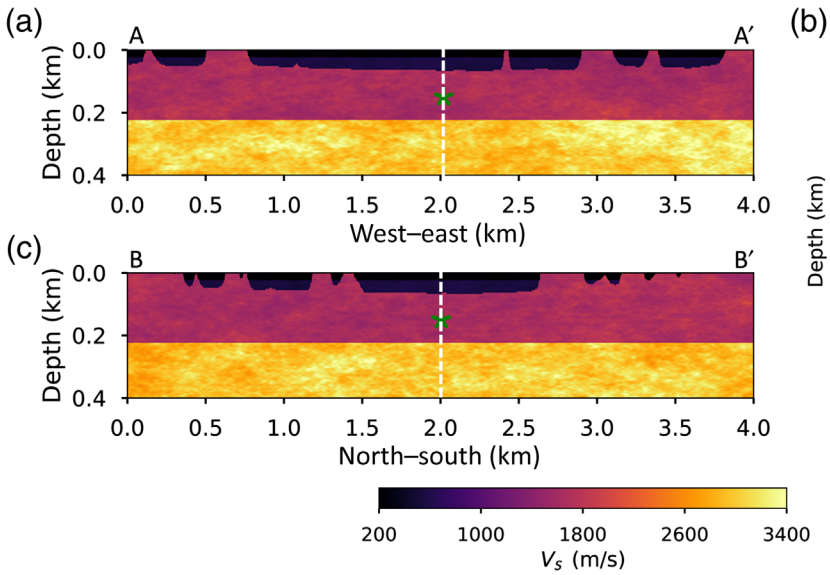

Figure 3. Cross sections of V_S in the 3D mesh (see Fig. 2) intersecting GVDA along (a) A–A′ and (c) B–B′; the downhole accelerometer is denoted with the asterisk. (b) The 1D V_S profile, with its location denoted by the dashed line in the left panels, obtained from the borehole log, and used in the SH1D model. The color version of this figure is available only in the electronic edition.

the upgoing waves in the simulations and to compute the TTF. The selection of event ID 33 was arbitrary for two reasons: (1) the ETFs at GVDA show low interevent source variability, indicated by the narrow $\pm 2\sigma$ band in Figure 4, and (2) the modeling is constrained to linear wave propagation. The use of a realistic source allows straightforward extension to multiple sites, as well as to nonlinear analysis in the future. The source time function was obtained by deconvolving the surface recordings of this event at the neighboring outcrop site GVAR (see Fig. 1) to the maximum depth of our domain.

The TTFs and ETFs for GVDA are compared in Figure 4. The two-sigma scatter

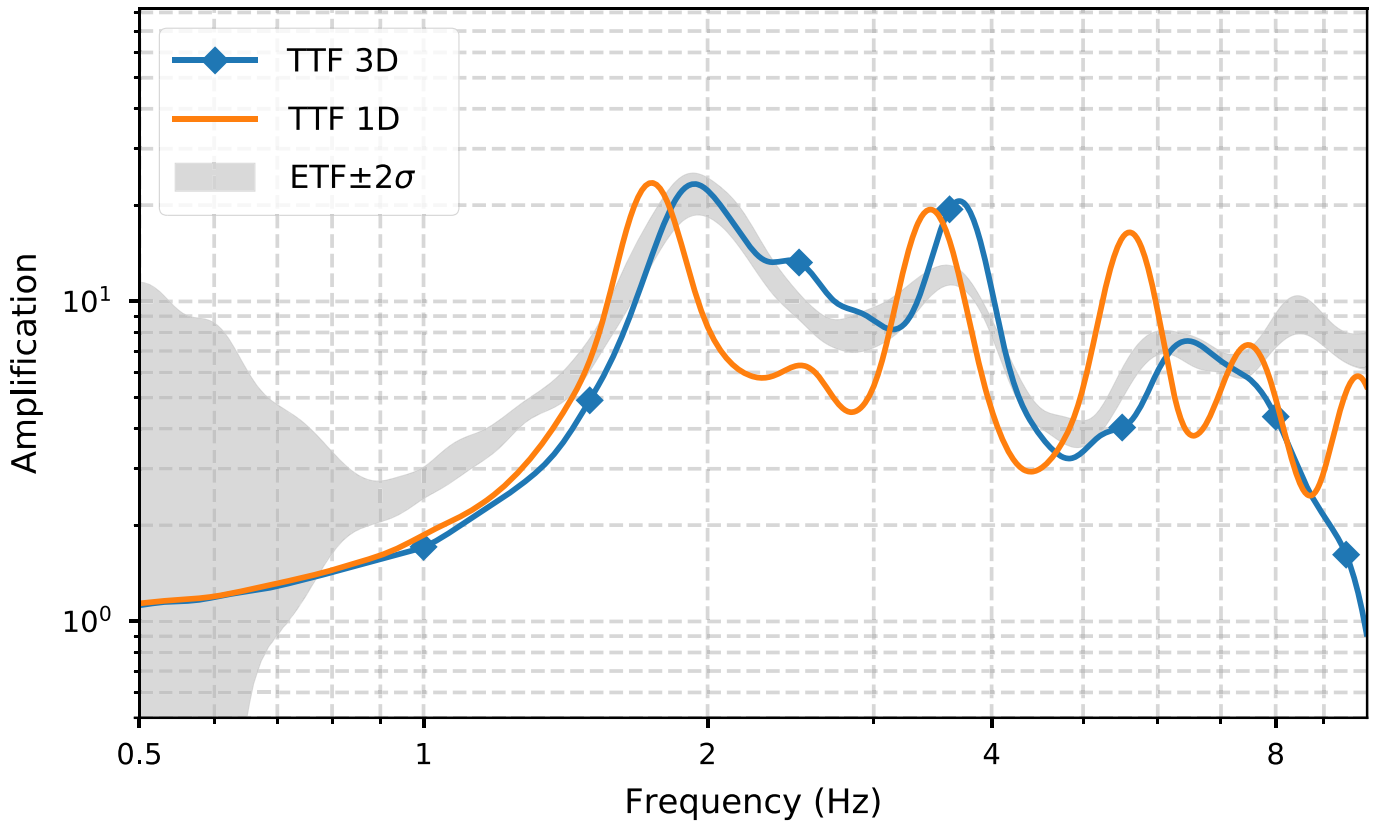

Figure 4. Comparison between the theoretical transfer functions (TTFs) computed using the 3D model and the SH1D model at GVDA, with the two-sigma scatter of empirical transfer functions (ETFs) shaded in gray. The color version of this figure is available only in the electronic edition.

TABLE 1
Earthquakes Used to Compute the Empirical Transfer Functions at Garner Valley Downhole Array (GVDA)

ID	Date (yyyy/mm/dd)	Time (hh:mm:ss)	M_L	Latitude (°)	Longitude (°)	Depth (km)	Distance (km)	Azimuth (°)
1	2007/06/02	05:11:26	4.3	33.8720	−116.2120	5	48	242
2	2007/06/13	14:50:34	3.4	33.6970	−116.0420	12	59	267
3	2008/07/29	18:42:16	5.4	33.9530	−117.7610	15	106	108
4	2008/12/06	04:18:43	5.1	34.8130	−116.4190	7	130	190
5	2009/03/13	03:42:22	3.0	34.0160	−117.1970	15	62	129
6	2009/11/15	07:54:23	3.3	33.9140	−117.0590	14	45	127
7	2010/03/13	16:32:32	4.2	32.9910	−116.3580	6	81	339
8	2010/06/15	04:26:58	5.7	32.7000	−115.9210	5	129	327
9	2010/07/08	01:07:11	3.0	33.4450	−116.4060	12	35	315
10	2010/11/17	09:46:15	3.2	33.9870	−117.1590	15	57	128
11	2011/06/14	08:25:41	3.6	33.6900	−116.7400	18	7	111
12	2011/11/19	20:32:21	3.9	33.2450	−116.2650	10	61	321
13	2012/03/30	06:09:27	3.3	33.3040	−116.8790	15	45	25
14	2012/05/18	10:37:12	3.6	33.3190	−116.4020	8	46	327
15	2012/08/08	16:33:22	4.5	33.9040	−117.7910	10	107	105
16	2012/08/27	04:41:37	4.9	33.0210	−115.5190	4	129	304
17	2012/10/02	08:28:15	4.1	32.8050	−116.1440	10	108	333
18	2013/03/11	16:56:06	4.7	33.5020	−116.4570	13	27	313
19	2013/03/27	17:50:29	3.4	33.4950	−116.4450	8	29	312
20	2014/01/16	07:40:06	3.6	33.8290	−117.6870	10	95	101
21	2014/03/29	04:09:42	5.1	33.9320	−117.9170	5	119	105
22	2014/05/19	20:08:52	3.8	34.2530	−116.8250	8	66	168
23	2014/07/10	20:41:44	3.2	33.5050	−116.5070	15	24	320
24	2014/11/03	08:53:35	3.3	34.0170	−117.2320	18	65	127
25	2014/12/04	16:53:21	3.6	33.9630	−116.6350	16	33	186
26	2015/05/31	13:02:56	3.6	33.3130	−116.2820	13	54	317
27	2016/01/09	11:43:11	3.3	33.6600	−116.7740	14	9	84
28	2016/02/14	09:01:10	3.4	33.8920	−117.1180	14	48	121
29	2016/06/10	08:04:39	5.2	33.4310	−116.4430	12	34	321
30	2016/09/26	14:31:08	4.3	33.2980	−115.7140	2	98	295
31	2017/06/25	13:53:25	3.5	34.0010	−116.9030	14	43	150
32	2017/12/09	20:45:24	3.5	33.4987	−116.8010	5	22	32
33	2018/04/23	00:46:09	3.9	33.9210	−116.3220	8	43	229
34	2018/05/19	19:26:51	3.5	33.4958	−116.8080	3	23	33
35	2018/08/04	13:48:49	3.1	33.9323	−116.8280	6	33	154
36	2018/09/01	16:50:29	3.1	33.4878	−116.8070	2	24	31

of all the ETFs is fairly narrow above 1 Hz and not sensitive to the azimuths and distances of the events, which implies that the ETFs are primarily determined by the site characteristics, and confers greater predictive power on an ETF (and presumably also on a TTF). Although the peaks for the ETFs and both 3D and 1D TTFs generally occur near the same frequencies, the goodness of fit predicted from the 1D model (VR = 0.64) is significantly smaller compared to the 3D model (VR = 0.85). This result suggests that the shallow 3D structure contributes first-order effects to the local site amplification at GVDA (see the Discussion section).

TKCH05

The KiK-net strong-motion seismograph network in Japan provides, approximately, 700 sites, with pairs of surface and downhole seismographs installed that have recorded earthquakes with a wide range of magnitudes. KiK-net also provides geological and geophysical data, including velocity structure for each site, derived from borehole logs. Thompson *et al.* (2012) analyzed the interevent variability and goodness of fit between SH1D models and data at 100 sites from KiK-net, and identified some sites where the standard 1D site response analysis provided poor results. Among these sites, we targeted TKCH05, which is located in Honbetsu, Hokkaido, Japan, to investigate the contributions from its underlying 3D structure on site effects. Figure 5 shows the location of TKCH05, in a narrow valley surrounded by mountains. The large gradients of the surface topography at the valley boundaries suggest the presence of significant 3D variation of the bedrock interface below the valley. The stratigraphy at TKCH05 is, approximately, 6 m of soil and sandy gravel with V_S = 140 m/s, overlying tens of meters of sandstone over gravel stone and siltstone (see Fig. 6; Natural Research Institute

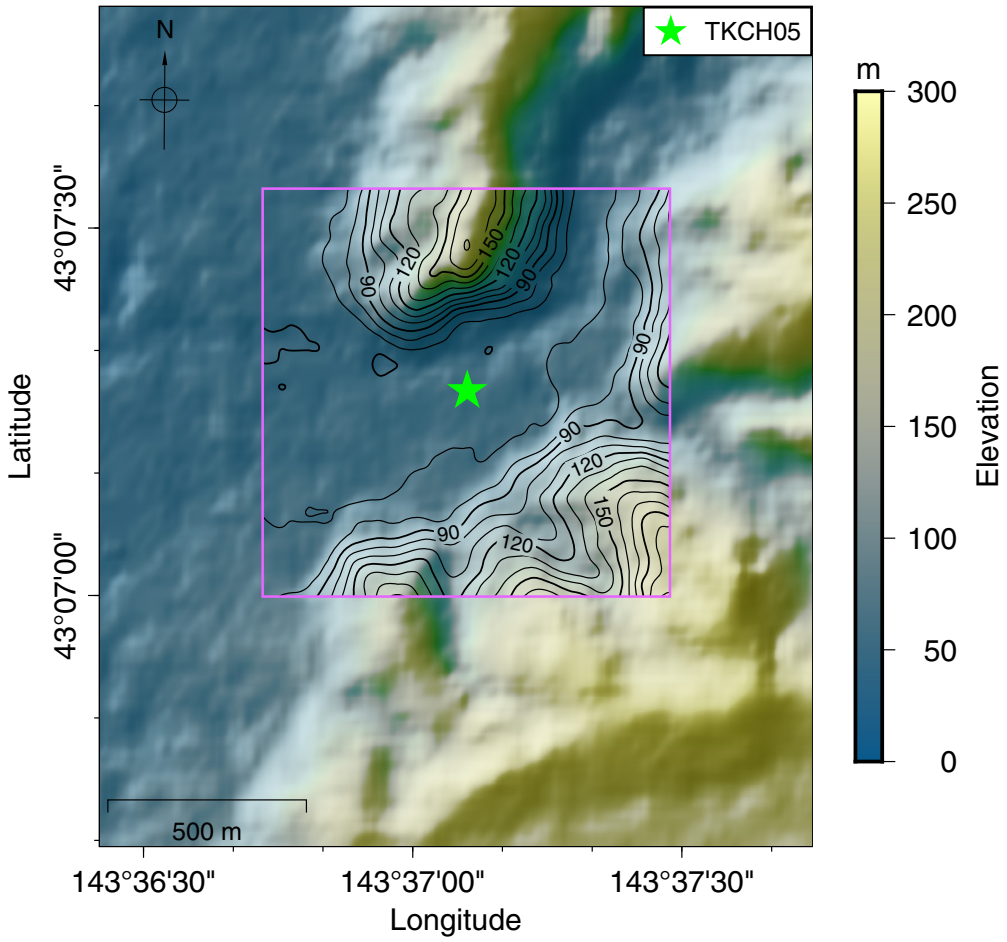

Figure 5. Site map of TKCH05, denoted by the star. The rectangle depicts the extent of the modeling domain, where the contours depict elevation in meters. The color version of this figure is available only in the electronic edition.

for Earth Science and Disaster Prevention [NIED], 2019). Table 2 lists the events included in our analysis of the ETFs at TKCH05 (see Fig. S2 for their locations and time series), among which the event with an ID of 1 was selected to generate the incoming waves in our simulations. As we did at site GVDA, we deconvolved the surface records at the closest outcrop site, F-net site URH, which is about 21.7 km away from TKCH05 to the domain bottom.

Figure 6 shows the downhole profile at TKCH05, and Figure 7a shows a comparison between the corresponding 1D TTF compared to the ETFs. The 1D TTF fails to match the frequency peaks and strongly overpredicts the amplifications at lower frequencies, producing a relatively low VR (VR = 0.35). We also considered the adjacent K-Net site HKD090, due to its proximity to TKCH05 (only 4 m relative distance), in our analysis. The available information from the measured V_S profile at HKD090 only extends to a depth of about 18 m, but, varies notably from those at TKCH05, considering the close distance. Because the top layers are as thin as 2 m, it is possible that the accuracy was degraded when the downhole logging measurements of travel time were converted to piecewise constant profiles. For this reason, we tested a simplified profile combining the two borehole logs, by replacing the TKCH05 V_S profile between 5 and 100 m, with an average value of 680 m/s. The adjustment reduces the strong discrepancy in shallow V_S values between the two borehole logs and retains the travel time from the bedrock to the surface. The SH1D model with the simplified profile produces a poorer fit to the ETF (VR = 0.181) than that obtained using the TKCH05 profile. Although, the simplified profile agrees better with the location of the second spectral peak of the ETF, the overall response compares less favorably to that obtained using the original profile due to larger amplitudes, especially at frequencies between 1 and 3 Hz.

Next, we extract our background 3D models at TKCH05 with a 1 km × 1 km × 1 km region, with the top boundary centered at TKCH05, from the Japanese national subsurface V_S model provided by J-SHIS. The J-SHIS model provides V_S and V_P and density with a horizontal spatial resolution of 1 km. Along the vertical direction, J-SHIS provides the depths of 33 layers with various thicknesses. Each layer is homogeneous and of increasing V_S with depth, ranging from 350 to 3400 m/s. Given the coarse horizontal resolution, the J-SHIS model is essentially 1D, with small stepwise discontinuities present close to the southern edge of the model (Fig. 8d). The bedrock depth was then estimated using the MRVBF method. The V_S below the downhole array is 1100 m/s, which increases to 1700 m/s at the bottom of our domain (Fig. 8). Based on the surface V_S of 140 m/s, we interpolated the initial mesh to a grid spacing of $\Delta h = 2.5$ m in the top partition of the mesh, to ensure at least 5–6 points per minimum S wavelength. In the discontinuous mesh setup, the lower mesh partition starts at a depth of 400 m, with a grid spacing of 7.5 m. Figure 7a compares ETFs to TTFs, based on the 3D models generated by the MRVBF technique, as well as the soil profile at TKCH05 and our simplified profile. Compared to the 1D models, the 3D models are able to fit the ETFs much better, with

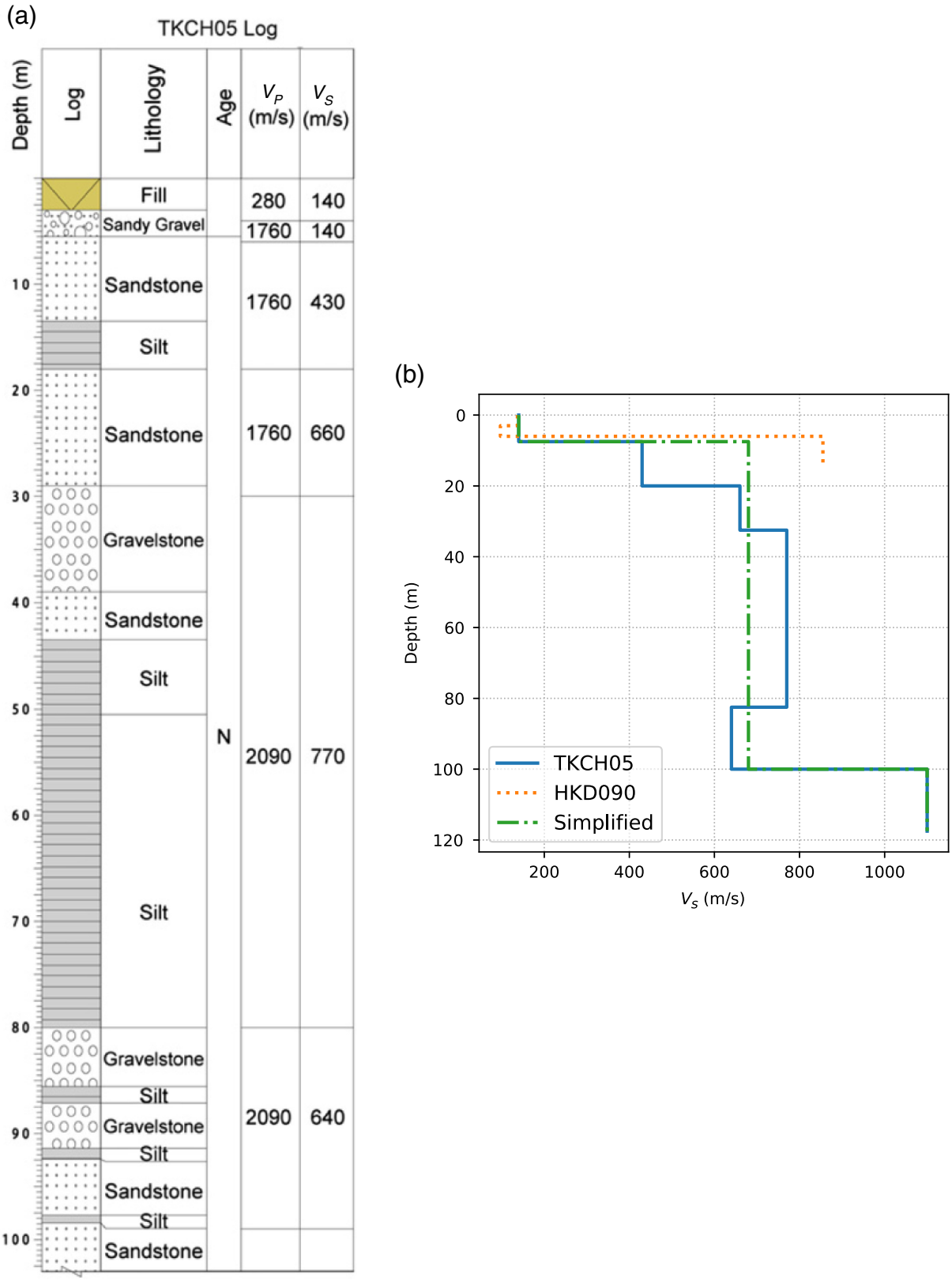

Figure 6. (a) Borehole log at TKCH05 (from Thompson *et al.*, 2012). (b) Borehole V_S profiles at TKCH05 and HKD090, as well as for our simplified 1D model. The color version of this figure is available only in the electronic edition.

TABLE 2
Earthquakes Used to Compute the Empirical Transfer Functions at TKCH05

ID	Date (yyyy/mm/dd)	Time (hh:mm:ss)	M_w	Latitude (°)	Longitude (°)	Depth (km)	Distance (km)	Azimuth (°)
1	2008/08/29	23:41:00	4.1	42.9350	144.0350	96	40	301
2	2008/11/09	09:11:00	3.8	42.7120	143.6980	93	46	352
3	2009/01/11	14:57:00	4.7	42.5930	143.4150	68	61	16
4	2009/02/28	09:36:00	5.3	42.5830	142.1880	113	131	63
5	2009/03/20	15:52:00	5.0	42.6000	144.5350	64	95	307
6	2009/06/05	12:30:00	6.4	41.8120	143.6200	31	145	360
7	2010/01/15	03:46:00	5.0	42.3520	143.1170	51	95	26
8	2010/04/09	03:41:00	4.8	42.9170	144.7220	57	93	284
9	2010/07/08	21:23:00	4.7	42.5730	144.5280	59	96	309
10	2010/07/28	08:06:00	4.5	42.3370	143.7980	56	88	350
11	2010/10/14	22:59:00	5.5	42.3120	143.0680	53	101	27
12	2012/03/11	17:33:00	4.4	42.5370	143.2650	63	71	24
13	2012/03/14	19:49:00	6.0	40.6800	144.9670	69	293	337
14	2012/07/22	13:42:00	5.1	42.4880	143.0250	61	85	35
15	2012/08/22	10:33:00	5.2	42.3470	143.0520	53	98	29
16	2012/10/26	19:52:00	3.7	42.7020	143.2120	104	57	36
17	2012/11/19	10:37:00	4.1	42.7730	143.9420	103	47	326
18	2013/03/09	21:16:00	5.0	43.1300	144.7700	101	94	269
19	2013/05/17	04:20:00	4.3	42.6720	143.4170	74	53	18
20	2013/08/22	15:53:00	4.8	42.3180	142.9950	54	103	30
21	2013/10/21	12:33:00	4.6	42.3200	143.0470	50	101	28
22	2014/04/21	16:46:00	4.2	42.4920	143.5630	77	70	4
23	2015/03/25	09:34:00	5.0	42.3520	143.0950	50	96	27
24	2015/08/14	13:43:00	5.1	42.7520	143.1120	80	58	45
25	2015/09/26	18:49:00	4.5	42.2120	141.9570	94	170	54
26	2015/11/11	00:50:00	3.9	42.9550	143.7580	116	22	328
27	2016/07/24	11:51:00	4.9	42.8730	143.1730	96	46	53
28	2016/09/07	18:42:00	4.7	42.4930	142.6800	110	104	48
29	2016/10/09	03:36:00	3.9	42.8770	143.9230	115	37	317
30	2016/10/12	04:02:00	5.0	42.3250	143.0420	50	100	28
31	2017/02/27	18:10:00	4.7	42.3480	143.0480	52	98	29
32	2017/03/14	12:57:00	4.7	42.8150	142.7000	82	82	66
33	2017/04/30	23:42:00	5.4	42.3220	143.0700	53	99	27
34	2017/09/10	17:44:00	5.6	41.7580	142.8770	43	163	22
35	2017/11/03	12:45:00	5.0	42.5630	143.7480	66	63	350
36	2018/04/14	04:00:00	5.4	43.1750	145.7370	53	172	267

VR values of 0.50 and 0.86 for the 3D models with the original and simplified profiles, respectively. The 3D models, while both producing a shift of the second peak compared with their corresponding 1D models, show remarkable improvement in the amplitudes of the first peak, especially when using the simplified profile. The results suggest that the simplified velocity profile, combining the borehole logs from the two adjacent sites, characterizes the local subsurface velocity structure below TKCH05 significantly better than the TKCH05 borehole log.

In general, a site response model can be evaluated by comparing the predicted surface ground motions (obtained by convolving the TF with the records at the reference site), with those recorded at the site of interest. We follow the traditional procedure for the calculation of TFs, neglecting the phase in the convolution process and quantifying the goodness of fit by the amplitudes only. Figure 7b,c compares the 1.5–8 Hz band-pass filtered surface recordings to the predicted motions from TTFs, illustrating the improvement in synthetic waveforms, as compared to data obtained at TKCH05 using the 3D as compared to the 1D model.

DISCUSSION

We have demonstrated for two borehole sites (GVDA and TKCH05) that site amplification estimation using TTFs can be significantly improved by including effects of the underlying 3D structure. However, the 3D TTFs still leave some room for improvement. A likely important cause of the remaining misfit between TTFs computed using 3D structure and the ETFs is the uncertainty in seismic velocity estimates as a function of depth. It is common practice in soil analysis to approximate the near-surface geology as a stack of layers with constant velocity. Boore and Thompson (2007) showed that the effects of approximating

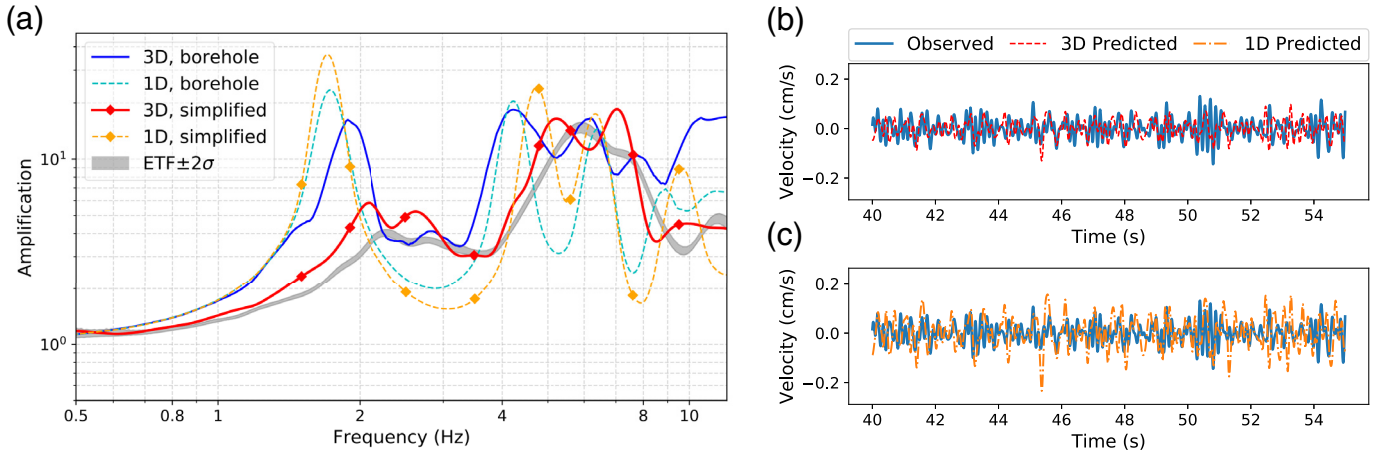

Figure 7. (a) Comparison between TTFs and the two-sigma scatter of the ETF for 3D and 1D models at TKCH05. Solid and dashed lines without markers are the 3D and 1D models based on the borehole log profile, respectively; solid and dashed lines with diamond markers depict the 3D and 1D models, based on the simplified downhole profile. (b,c) Comparison of 1.5–8 Hz observed east–west component surface ground motions with those obtained from convolution of the downhole records with the TTFs from models using the simplified profile for the (b) 3D model and (c) 1D model. The color version of this figure is available only in the electronic edition.

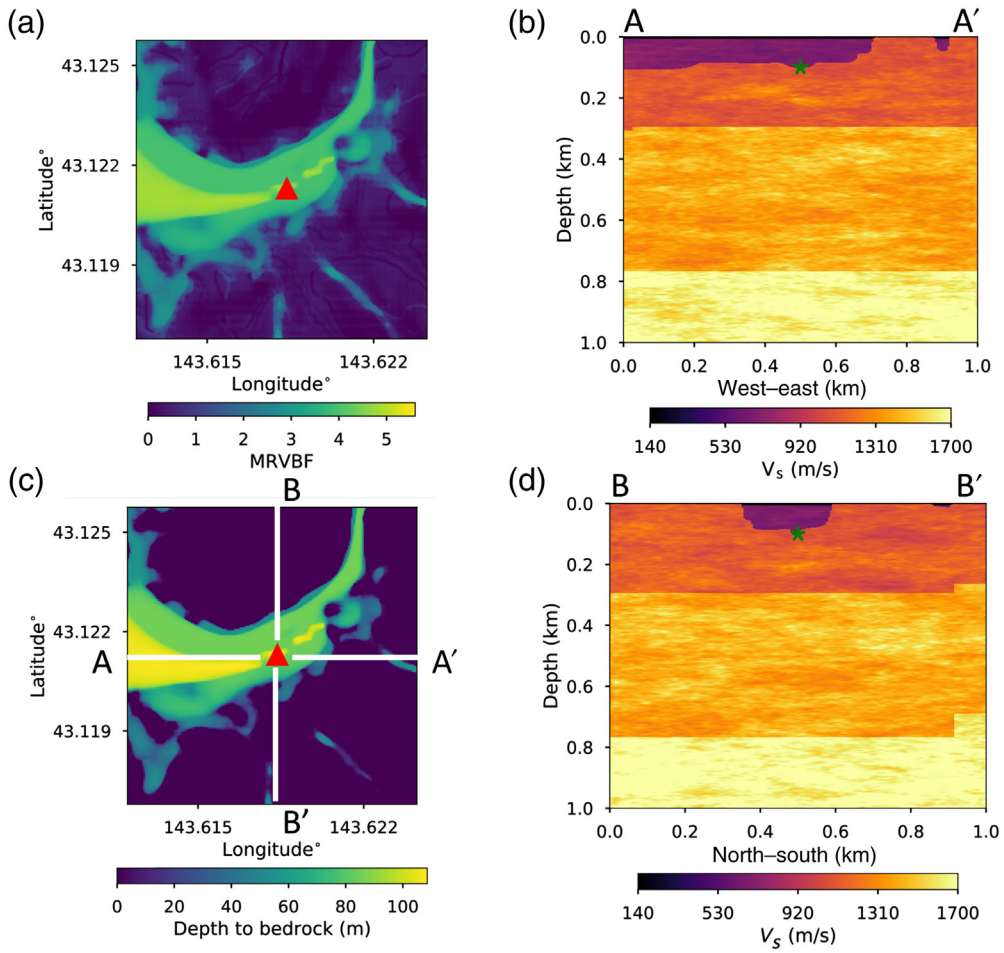

Figure 8. (a) MRVBF and (c) depth to bedrock in the vicinity of TKCH05, with the site location denoted by the triangle. (b) West–east A–A′ and (d) north–south B–B′ cross sections intersecting TKCH05, the downhole sensor is marked with the asterisk. The color version of this figure is available only in the electronic edition.

logging measurements with 10 m thick, constant-slowness layers are small for frequencies less than about 5 Hz. However, Day (1996) examined analytically the relation between site response in the frequency domain and elastic structure and found that the spectral average of bandwidth Δf is only constrained by the elastic structure up to a two-way traveltime depth of $1/\Delta f$. This means that the average TF (predominantly at higher frequencies) can be biased due to uncertainty in the shallow structure. Because the first layer is often thin, a bias in the thickness estimate can contribute relatively large error in the site effects.

The deeper structure, in particular, the bedrock depth, can also be important in determining the TFs. In conventional 1D models, the bedrock topography is simplified as a layer with fixed depth; whereas, our approach incorporates lateral variations by mapping surface topography. The subsurface

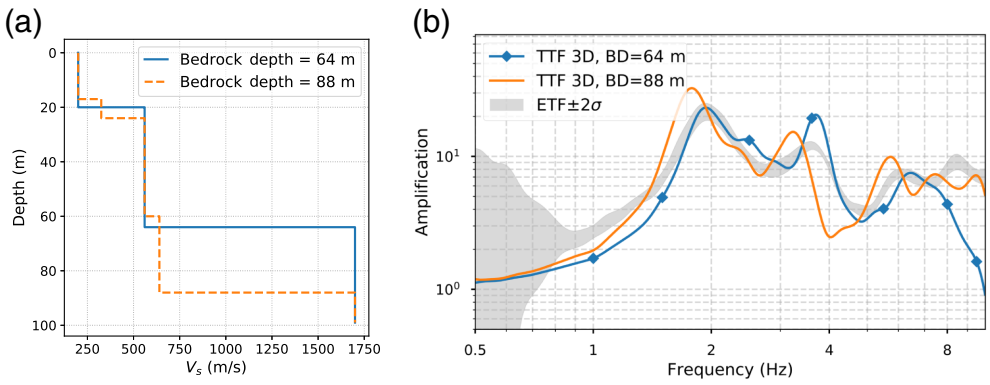

Figure 9. (a) The Gibbs and Steller velocity profiles at GVDA, in which the bedrock depth is 64 (solid line) and 88 m (dashed line), respectively. (b) Comparison between the two-sigma scatter of the ETFs (gray shaded) and the TTFs from the 3D models assembled with the Gibbs and Steller profiles, respectively. The color version of this figure is available only in the electronic edition.

structure in our model is, therefore, composed of multiple irregular interfaces, each of which is anchored to the borehole log right beneath the site of interest. In some cases, the exact depth of the soil-bedrock interface is unclear. For example, the weathered granite boundary below the GVDA site is reported at 64 m by Gibbs (1989) and 87 m by Steller. The two velocity profiles are similar, except for the bedrock depth (Fig. 9a). In the following discussion, the two models utilize their respective bedrock depth and velocity profiles. Figure 9b shows the TFs from two 3D models assembled with the Gibbs and Steller profiles (the latter shifted 1 m deeper than the reported value due to the 4 m spatial resolution of our model). The Steller model response matches the ETF at high frequencies better than that from the Gibbs model, whereas, the latter model fits better at 1.5–7 Hz, with a slightly better overall fit (VR = 0.85 vs. 0.82). It is noticeable that the Steller model, representing lower average velocity in the soil column, results in a shift of the peaks of the TF to the left at low frequencies. We conclude that both the lateral variation and the location of the subsurface strata are important in modeling the site response. The 3D-to-1D comparison shown in Figure 4 indicates that the lateral variations lead to changes in both the amplitudes and the frequency of the TF, whereas the variability of the bedrock depth mainly results in shifts in frequency of the TF.

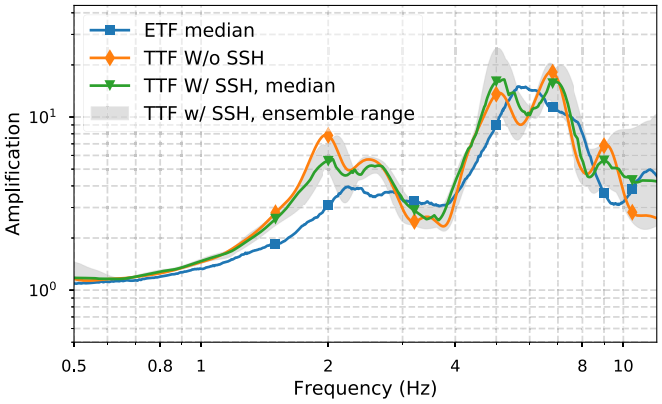

Figure 10. Comparison between the median ensemble ETF, the TTF from the 3D model without and with small-scale heterogeneities (SSHs) at TKCH05. The gray shaded region is the range of maximum and minimum values encountered in TTFs from these realizations of SSHs. The color version of this figure is available only in the electronic edition.

Another source of uncertainty in the site amplification estimates arises from unconstrained (mostly high frequency) scattering effects from crustal SSHs, and we test the effects thereof from a range of different parameters of the von Karman autocorrelation functions. Figure 10 shows the 3D TTFs modeled with a nine-realization ensemble of von Karman velocity and density perturbations, by varying the Hurst number from 0.05 to 0.15, the correlation length from 50 to 500 m, and the standard deviation of 5% and 10%, while keeping the horizontal-to-vertical anisotropy at 5. We find that the TTFs computed from these 3D models are relatively insensitive to the SSHs, except near the upper limit of our modeling bandwidth ($> \sim 9$ Hz). The median VR (0.83) of the resulting TTFs is similar to that without including the SSHs, suggesting that the random fields do not contribute first-order effects to the site amplification. However, our sensitivity study included only limited realizations for each set of von Karman parameters due to computational limitations, and, we recommend a more thorough analysis, estimating the uncertainty of the site amplification estimates arising from additional ensembles of statistical distributions of small-scale crustal perturbations.

To better understand the reasons why the 3D models better predict the observed site amplification, as compared to their 1D counterparts, we show snapshots of wave propagation for our 3D and 1D (simplified) models of TKCH05 in Figures S3 and S4. The snapshots are extracted for frequencies between 4.5 and 5 Hz, in which the 3D TTF provides a much improved fit to the ETF, as compared to the 1D TTF. As expected, the 3D models naturally increase the complexity of the wave propagation compared to the SH1D model, for example, the presence of wave energy trapped in basins, and reflections at interfaces between geological units with different V_S (Fig. S3). For example, note the horizontally propagating energy in the upper tens of meters in the snapshots from the 3D model,

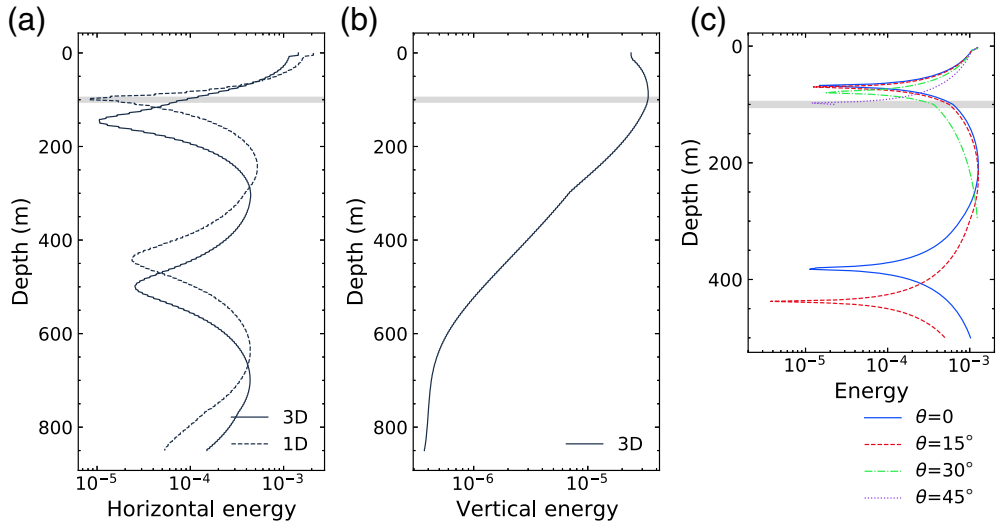

Figure 11. Energy on the (a) horizontal and (b) vertical components at the site TKCH05. (c) Total energy along depth using the simplified velocity profile at TKCH05 with different incidence angles. The gray horizontal line, at around 100 m depth, depicts the downhole site depth. The color version of this figure is available only in the electronic edition.

naturally absent in the 1D results. Of course, the improvement in the site response from the 3D model depends on the accuracy of the added degrees of freedom.

To further illustrate this added complexity, we compare the horizontal and vertical cumulative energy along the borehole profile (Fig. 11a,b) to the theoretical (1D) response (Fig. 11c) for different incidence angles at TKCH05. We carry out our analysis for the bandwidth 1.6–1.9 Hz, centered on the largest SH1D ETF peak at about 1.75 Hz (see Fig. 7a). The depth-dependent theoretical particle velocities, with the internal reflections neglected, can be described as follows:

$$v(z,t) = \cos\left(\omega\left(t - \frac{z\cos\theta}{V_s}\right)\right) + \cos\left(\omega\left(t + \frac{z\cos\theta}{V_s}\right)\right), \quad (6)$$

in which z is the depth, t is the time, ω is the angular frequency, and θ is the incidence angle. As inferred from the SH1D solution in Figure 11c, the peak at ~1.75 Hz is, primarily, due to a node at the downhole sensor location in the vertical-incidence response. This theoretical solution implies that a small departure from vertical incidence, which, in practice, is caused by interactions with the 3D bedrock interface, scatters some vertically propagating seismic waves to obliquely propagating waves, and moves the node to greater depth, thereby, increasing the response at the sensor depth point. Such wave scattering changes the energy distribution along depth, including the reduced horizontal-component energy near a depth of 100 m in the 3D model compared to the 1D model (Fig. 11a) and the increase in vertical-component energy (Fig. 11b). The results indicate that at TKCH05, the site response remains a first-order 1D resonance effect, but coupled with 3D effects from horizontally propagating waves, which, when included, greatly improves the fit to the ETF compared with the SH1D model.

SUMMARY AND CONCLUSIONS

We present a method to obtain refined site effect measurements by taking into account 3D structural variation below a downhole array site and a path to refine estimates of the elastic properties of the underlying stratigraphy via the MRVBF technique. The approach requires layer properties (e.g., *S*-wave velocities) along a vertical profile (typically obtained from the downhole array) as well as regional elevation data, which is widely available for most areas.

Application of the method to two sites, GVDA in southern California and TKCH05 in Japan, illustrates the extent of improvement over the conventional 1D site effect amplifications that can be expected. The relatively poor fit of the SH1D model at TKCH05 indicates that it deviates strongly from 1D behavior, supported by the complex 3D structure in the vicinity of the downhole array obtained by the MRVBF technique. Although significant improvement of the fit was obtained at GVDA as well, our results suggest that the medium below the borehole site is more horizontally stratified than is the case at TKCH05 (smaller improvements from including the effects of a MRVBF-estimated 3D model). This interpretation is also supported by the horizontally stratified nature of the resulting 3D model around the GVDA site, except for smaller patches of near-surface low-velocity material produced by the method.

Thus, our method is likely to improve the prediction of site response in the presence of significant 3D structure, as well as at sites with an oversimplified or otherwise less accurate V_S profile. However, the accuracy of the site effects estimated by our proposed technique depends strongly on the fidelity of the available soil properties in the borehole, in particular at the upper end of our target bandwidth, near 10 Hz. The variability of the bedrock depth, beneath the site, as one of the controlling parameters in constructing our 3D model, can be a significant source of error in the prediction of the TF, by introducing frequency shifts at low frequencies. Finally, our results show that the improvement of the TTFs produced by incorporating small-scale crustal heterogeneities via a statistical model is secondary to that obtained by including 3D subsurface information.

Our results generally support the conclusions by Thompson *et al.* (2009) that the theoretical formulation to map soil properties to site amplification largely limits our ability to accurately model site response transfer functions, rather than the uncertainties of the soil property. However, our method provides a realistic constitutive framework, suitable for predicting site response, regardless of the spatial variability in material properties across the site. Furthermore, this approach can be extended to explore nonlinear soil effects, another important component of site effects not explored here. For future work, we also recommend that the assumption of the quantitative relationship between topography and bedrock depth receive further scrutiny with 3D simulations at more sites, especially where the interevent variability is large.

DATA AND RESOURCES

The seismograms and borehole log data used in this study were collected from the National Research Institute for Earth Science and Disaster Prevention (NIED, 2019) in Japan for TKCH05, and the Earthquake Engineering Group, Earth Research Institute at University of California, Santa Barbara (UCSB) (http://nees.ucsb.edu/) for Garner Valley Downhole Array (GVDA). The transfer functions for all earthquakes and simulations at both sites used in the analysis can be obtained from the authors upon request. Some plots were made using the Generic Mapping Tools (GMT) version 6.0.0 (https://www.generic-mapping-tools.org/; Wessel *et al.*, 2019). We used the open-source project ObsPy version 1.2.0 (https://github.com/obspy/obspy) to compute the Konno–Ohmachi smoothing window for Transfer functions (TFs). All websites were last accessed in June 2020. We included figures on the event locations and recorded accelerations, as well as snapshots of the 3D and 1D simulations, for GVDA and TKCH05 in the supplemental material to this article.

ACKNOWLEDGMENTS

Computations in this project were performed on Rhea and Summit, which are part of the Oak Ridge Leadership Facility at the Oak Ridge National Laboratory. This research was supported by the Southern California Earthquake Center (SCEC; Contribution Number 10885) and by the National Science Foundation under Grant Number EAR-1664203. SCEC is funded by National Science Foundation (NSF) Cooperative Agreement EAR-1600087 and U.S. Geological Survey (USGS) Cooperative Agreement G17AC00047. Figure 6a is reprinted from Thompson *et al.* (2012). The authors thank two anonymous reviewers and the Associate Editor Jim Kaklamanos for valuable suggestions that helped to improve this article.

REFERENCES

Abrahamson, N., and W. Silva (2008). Summary of the Abrahamson & Silva NGA ground-motion relations, *Earthq. Spectra* **24,** no. 1, 67–97.

Akkar, S., and J. J. Bommer (2010). Empirical equations for the prediction of PGA, PGV, and spectral accelerations in Europe, the mediterranean region, and the Middle East, *Seismol. Res. Lett.* **81,** no. 2, 195–206.

Archuleta, R., S. Seale, and L. B. S. Swain (1992). Garner Valley downhole array of accelerometers: Instrumentation and preliminary data analysis, *Bull. Seismol. Soc. Am.* **82,** no. 4, 1592–1621.

Atik, L. A., N. Abrahamson, J. J. Bommer, F. Scherbaum, F. Cotton, and N. Kuehn (2010). The variability of ground-motion prediction models and its components, *Seismol. Res. Lett.* **81,** no. 5, 794–801.

Atkinson, G. M., and D. M. Boore (2006). Earthquake ground-motion prediction equations for eastern North America, *Bull. Seismol. Soc. Am.* **96,** no. 6, 2181–2205.

Barani, S., R. De Ferrari, and G. Ferretti (2013). Influence of soil modeling uncertainties on site response, *Earthq. Spectra* **29,** no. 3, 705–732.

Beresnev, I. A., and K.-L. Wen (1996). Nonlinear soil response a reality? *Bull. Seismol. Soc. Am.* **86,** no. 6, 1964–1978.

Bonilla, L. F., J. Steidl, J.-C. Gariel, and R. Archuleta (2002). Borehole response studies at the Garner Valley downhole array, southern California, *Bull. Seismol. Soc. Am.* **92,** no. 8, 3165–3179.

Boore, D. M. (2004). Can site response be predicted? *J. Earthq. Eng.* **8,** no. sup001, 1–41.

Boore, D. M., and E. M. Thompson (2007). On using surface-source downhole-receiver logging to determine seismic slownesses, *Soil Dynam. Earthq. Eng.* **27,** no. 11, 971–985.

Borcherdt, R. D. (1970). Effects of local geology on ground motion near San Francisco Bay, *Bull. Seismol. Soc. Am.* **60,** 29–61.

Building Seismic Safety Council (BSSC) (2003). *The 2003 NEHRP Recommended provisions for new buildings and other structures. Part 1: Provisions (FEMA 450)*, Federal Emergency Management Agency, Washington, D.C.

Chávez-García, F. J., and E. Faccioli (2000). Complex site effects and building codes: Making the leap, *J. Seismol.* **4,** no. 1, 23–40.

Cui, Y., K. B. Olsen, T. H. Jordan, K. Lee, J. Zhou, P. Small, D. Roten, G. Ely, D. K. Panda, A. Chourasia, *et al.* (2010). Scalable earthquake simulation on petascale supercomputers, *2010 ACM/IEEE International Conf. for High Performance Computing, Networking, Storage and Analysis*, New Orleans, Los Angeles, IEEE, 1–20.

Day, S. M. (1996). RMS response of a one-dimensional half-space to SH, *Bull. Seismol. Soc. Am.* **86,** no. 2, 363–370.

Field, E. H., and K. H. Jacob (1995). A comparison and test of various site-response estimation techniques, including three that are not reference-site dependent, *Bull. Seismol. Soc. Am.* **85,** no. 4, 1127–1143.

Frankel, A., and R. W. Clayton (1986). Finite difference simulations of seismic scattering: Implications for the propagation of short-period seismic waves in the crust and models of crustal heterogeneity, *J. Geophys. Res.* **91,** no. B6, 6465.

Gallant, J. C., and T. I. Dowling (2003). A multiresolution index of valley bottom flatness for mapping depositional areas, *Water Resour. Res.* **39,** no. 12, 1347.

Gibbs, J. F. (1989). Near-surface P- and S-wave velocities from borehole measurements near lake Hemet, California, *U.S. Geol. Surv. Open-File Rept. 89-630*, available at https://pubs.er.usgs.gov/publication/ofr89630 (last accessed June 2020).

Griffiths, S. C., B. R. Cox, E. M. Rathje, and D. P. Teague (2016). Mapping dispersion misfit and uncertainty in Vs profiles to variability in site response estimates, *J. Geotech. Geoenviron. Eng.* **142,** no. 11, 04016062.

Hill, R. (1981). Geology of garner valley and vicinity, *South Coast Geol. Soc.* 90–99.

Idriss, I. M. (2014). An NGA-West2 empirical model for estimating the horizontal spectral values generated by shallow crustal earthquakes, *Earthq. Spectra* **30,** no. 3, 1155–1177.

Konno, K., and T. Ohmachi (1998). Ground-motion characteristics estimated from spectral ratio between horizontal and vertical

components of microtremor, *Bull. Seismol. Soc. Am.* **88,** no. 1, 228–241.
Kramer, S. L. (1996). *Geotechnical Earthquake Engineering*, Prentice Hall, Englewood Cliffs, New Jersey.
Matavosic, N., and Y. Hashash (2012). *Practices and Procedures for Site-Specific Evaluations of Earthquake Ground Motions*, Transportation Research Board, Washington, D.C.
Nakajima, J., S. Hada, E. Hayami, N. Uchida, A. Hasegawa, S. Yoshioka, T. Matsuzawa, and N. Umino (2013). Seismic attenuation beneath northeastern Japan: Constraints on mantle dynamics and arc magmatism, *J. Geophys. Res.* **118,** no. 11, 5838–5855.
Natural Research Institute for Earth Science and Disaster Prevention (NIED) (2019). National Research Institute for Earth Science and Disaster Resilience, *NIED K-NET KiK-Net Natl. Res. Inst. Earth Sci. Disaster Resil*, available at https://www.kyoshin.bosai.go.jp/ (last accessed June 2020).
Nie, S., Y. Wang, K. B. Olsen, and S. M. Day (2017). Fourth-order staggered-grid finite-difference seismic wavefield estimation using a discontinuous mesh interface (WEDMI), *Bull. Seismol. Soc. Am.* **107,** no. 5, 2183–2193.
Nour, A., A. Slimani, N. Laouami, and H. Afra (2003). Finite element model for the probabilistic seismic response of heterogeneous soil profile, *Soil Dynam. Earthq. Eng.* **23,** no. 5, 331–348.
Olsen, K. B. (1994). *Simulation of Three Dimensional Wave Propagation in the Salt Lake Basin*, The University of Utah, Salt Lake City, Utah.
Olsen, K. B., and G. T. Schuster (1995). Causes of low-frequency ground motion amplification in the Salt Lake Basin: The case of the vertically incident P wave, *Geophys. J. Int.* **122,** no. 3, 1045–1061.
Roten, D., D. Fäh, K. B. Olsen, and D. Giardini (2008). A comparison of observed and simulated site response in the Rhône valley, *Geophys. J. Int.* **173,** no. 3, 958–978.
Roten, D., K. B. Olsen, and J. C. Pechmann (2012). 3D simulations of M 7 earthquakes on the Wasatch Fault, Utah, Part II: Broadband (0-10 Hz) ground motions and nonlinear soil behavior, *Bull. Seismol. Soc. Am.* **102,** no. 5, 2008–2030.
Savran, W. H., and K. B. Olsen (2016). Model for small-scale crustal heterogeneity in Los Angeles basin based on inversion of sonic log data, *Geophys. J. Int.* **205,** no. 2, 856–863.
Savran, W. H., and K. B. Olsen (2019). Ground motion simulation and validation of the 2008 Chino Hills earthquake in scattering media, *Geophys. J. Int.* **219,** no. 3, 1836–1850.
Shearer, P. M., and J. S. Orcutt (1987). Surface and near-surface effects on seismic waves—Theory and borehole seismometer results, *Bull. Seismol. Soc. Am.* **77,** no. 4, 1168–1196.
Small, P., D. Gill, P. J. Maechling, R. Taborda, S. Callaghan, T. H. Jordan, K. B. Olsen, G. P. Ely, and C. Goulet (2017). The SCEC unified community velocity model software framework, *Seismol. Res. Lett.* **88,** no. 6, 1539–1552.
Steidl, J. H. (1993). Variation of site response at the UCSB dense array of portable accelerometers, *Earthq. Spectra* **9,** no. 2, 289–302.
Steidl, J. H., A. G. Tumarkin, and R. J. Archuleta (1996). What is a reference site? *Bull. Seismol. Soc. Am.* **86,** no. 6, 1733–1748.
Steller, R. (1996). New borehole geophysical results at GVDA, *UCSB Internal Report*, available at http://nees.ucsb.edu/sites/eot-dev.nees.ucsb.edu/files/facilities/docs/GVDA-Geotech-Stellar1996.pdf (last accessed June 2020).
Tao, Y., and E. Rathje (2019). Insights into modeling small-strain site response derived from downhole array data, *J. Geotech. Geoenviron. Eng.* **145,** no. 7, 04019023.
Tao, Y., and E. Rathje (2020). Taxonomy for evaluating the site-specific applicability of one-dimensional ground response analysis, *Soil Dynam. Earthq. Eng.* **128,** 105,865.
Teague, D. P., B. R. Cox, and E. M. Rathje (2018). Measured Vs. predicted site response at the Garner Valley Downhole Array considering shear wave velocity uncertainty from borehole and surface wave methods, *Soil Dynam. Earthq. Eng.* **113,** 339–355.
Thompson, E. M., L. G. Baise, R. E. Kayen, and B. B. Guzina (2009). Impediments to predicting site response: Seismic property estimation and modeling simplifications, *Bull. Seismol. Soc. Am.* **99,** no. 5, 2927–2949.
Thompson, E. M., L. G. Baise, Y. Tanaka, and R. E. Kayen (2012). A taxonomy of site response complexity, *Soil Dynam. Earthq. Eng.* **41,** 32–43.
Toro, G. (1995). Probabilistic models of site velocity profiles for generic and site-specific ground-motion amplification studies, *Technical Report No. 779574*, Brookhaven National Laboratory, Upton, New York, 147 pp.
Wessel, P., J. F. Luis, L. Uieda, R. Scharroo, F. Wobbe, W. H. F. Smith, and D. Tian (2019). The generic mapping tools version 6, *Geochem. Geophys. Geosys.* **20,** no. 11, 5556–5564.
Withers, K. B., K. B. Olsen, and S. M. Day (2015). Memory-efficient simulation of frequency-dependent *q*, *Bull. Seismol. Soc. Am.* **105,** no. 6, 3129–3142.
Withers, K. B., K. B. Olsen, S. M. Day, and Z. Shi (2019). Ground motion and intraevent variability from 3D deterministic broadband (0–7.5 Hz) simulations along a nonplanar strike-slip fault, *Bull. Seismol. Soc. Am.* **109,** no. 1, 229–250.
Zhu, C., E. Riga, K. Pitilakis, J. Zhang, and D. Thambiratnam (2018). Seismic aggravation in shallow basins in addition to one-dimensional site amplification, *J. Earthq. Eng.* **24,** no. 9, 402–412.

APPENDIX

The form of the Von Karman autocorrelation function (Frankel and Clayton, 1986) is

$$\Phi_{v,a}(r) = \sigma^2 \frac{2^{1-\nu}}{\Gamma(\nu)} \left(\frac{r}{a}\right)^{\nu} K_{\nu}\left(\frac{r}{a}\right), \tag{A1}$$

in which ν is the Hurst component, a is the correlation length, K_{ν} is the modified Bessel function of order ν, $\Gamma(\nu)$ is the gamma function, and σ^2 is the variance with Fourier transform:

$$P(k) = \frac{\sigma^2 (2\sqrt{\pi}a)^E \Gamma(\nu + E/2)^{\nu+E/2}}{\Gamma(\nu)(1 + k^2 a^2)}, \tag{A2}$$

in which E is the Euclidean dimension.

Manuscript received 17 June 2020
Published online 16 February 2021